Combining experiments and modelling to predict the competition between liquid spreading and impregnation in porous media for Metal Binder Jetting applications

Romain Ravel, Monica Francesca Pucci, Synthia Divin, Benoît Verquin, Christophe Reynaud, Julien Bruchon, Pierre-Jacques Liotier

Combining experiments and modelling to predict the competition between liquid spreading and impregnation in porous media for Metal Binder Jetting applications

Romain Ravel [a], Monica Francesca Pucci [b], Synthia Divin [c], Benoît Verquin [d], Christophe Reynaud [d], Julien Bruchon [c], Pierre-Jacques Liotier [a,*]

[a] *Polymers Composites and Hybrids (PCH), IMT Mines Ales, Ales, France*
[b] *LMGC, IMT Mines Ales, Univ Montpellier, CNRS, Ales, France*
[c] *Mines Saint-Étienne, Université de Lyon, CNRS, UMR 5307 LGF, Centre SMS - 158 Cours Fauriel 42023, Saint-Étienne, France*
[d] *Cetim, 7 Rue de la Presse, 42000 Saint-Étienne, France*

GRAPHICAL ABSTRACT

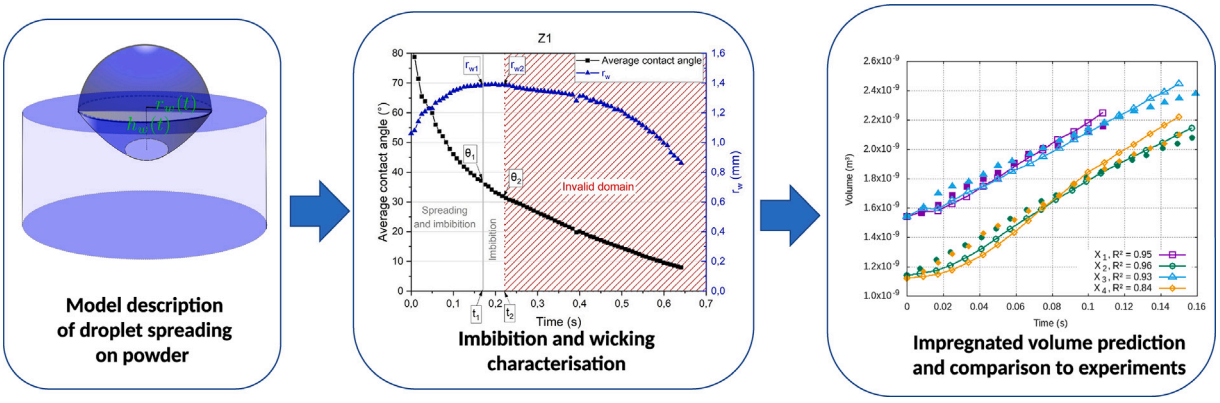

ABSTRACT

A predictive model accounting for binder spreading and impregnation in powders during Metal Binder Jetting was set. Presintered cylindrical samples were 3D printed considering main printing orientations and two types of wetting tests were carried out on samples : imbibition or wicking tests using a tensiometric method and spreading-impregnation tests using a sessile drop method with a goniometer. Tensiometric tests showed results on impregnation rate in powders and goniometric tests gave the impregnated volume of the binder drop into the powder. Both those experiments allowed to identify physical parameters depending on the binder and powder bed interaction. All parameters injected in the model have been identified in the present study. The proposed model accurately described experiments and showed the dependence of impregnated volume on wetting parameters but also on printing orientation.

Keywords:
Spreading
Impregnation
Powder
Metal binder jetting

1. Introduction

Metal Binder Jetting (MBJ) is an additive manufacturing (AM) process in which the metal powder is spread along a main direction to form a layer and binder droplets, or liquid bonding agent droplets, are deposited on the powder bed in order to join the powder material. Layer by layer, a "green part" is indeed 3D printed by the deposition of binder drops. Steps of curing, "depowdering", sintering and eventually

* Corresponding author.
E-mail address: pierre-jacques.liotier@mines-ales.fr (P.-J. Liotier).

finishing follow the printing step to obtain the final part [1]. This technology has a great potential compared to other AM processes, like powder bed fusion techniques, because of the high production rate of complex parts without significant heating during printing and controlling part density during sintering [2,3]. However, as for other techniques, the quality of printing during MBJ depends on a lot of parameters. Parameters of MBJ printing are related to the wetting of binder drops on the powder bed. More specifically, binder (or ink) droplets spread on (horizontal binder migration) and impregnate (vertical binder migration) the powder bed and these phenomena will be driven by capillary effects, gravity effects being negligible due to the very low binder drop volume [3]. These capillary phenomena will depend on the binder nature itself, the droplets shape and spacing, the powder characteristics and distribution, as well as on the physico-chemical interactions between binder and powder bed [4–6]. The deposition rate, or print head speed, and the possible distortion of the powder bed due to the drop impact can also have an effect [7].

The understanding of these phenomena for MBJ process is of first importance since it has been proved that the strength of green parts depends on the print steps and the saturation level of binder in powder [8,9] leading to complex residual stress field during curing [10]. Some experimental studies were carried out and models were proposed to predict the drop penetration time on powder beds [11] or a saturation degree in powder [12]. Models adapted for droplet spreading on honeycomb, considered as vertical tubes, have been used by Denesuk et al. [13,14]. Those studies have been used to build approaches for MBJ and define some limitations in the binder behaviour since it is a polymer solution [15–17]. Moreover, some studies focused on powder wettability trough capillary rise, using the Washburn theory [18–20]. Experiments of sessile drops and capillary rise were also carried out in order to relate the capillary pressure to the saturation degree [21] or to find a saturation optimum [22]. On the other hand, numerical models of drop spreading and micro-impregnation were also proposed in literature [23–26].

The aim of the present work is to understand how the binder, or ink, fills the space between powders for MBJ processes. Therefore, this study focuses on the interactions between the powder and the binder and its originality consists in combining experiments and modelling of both spreading and impregnation on porous materials. A model is proposed consisting in the description of two coupled phenomena, spreading of the droplet at the surface of the powder bed and impregnation into the powder bed, in order to estimate an impregnated volume. The impregnated volume is defined by the liquid volume into the powder bed and it can be very different if one of two phenomena prevails on the other. Indeed, the competition between phenomena can result in a large wet area with a low depth of impregnation or in a relatively small wet area with a high depth of impregnation, as shown in Fig. 1. An optimum between extreme possible configurations (Fig. 1a and b) might exist and the model to predict impregnated volume will be determinant to identify the optimum depending on ink and powder wetting parameters. Tensiometric tests were set on samples in order to obtain wetting parameters affecting impregnation and goniometric tests allowed to determine characteristic volumes depending on drop spreading radius and contact angles as a function of time. Thanks to experiments combined to the modelling, the effect of print orientation on the spreading and impregnation and thus on the impregnated volume, was highlighted.

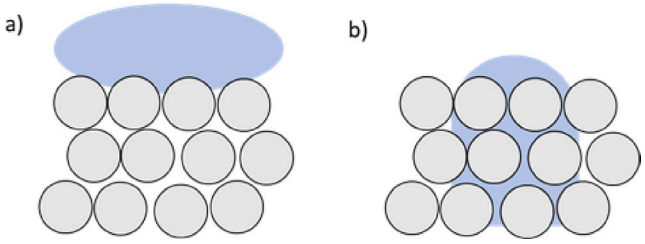

Fig. 1. Extreme possible configurations of wetting: (a) high spreading and low impregnation; (b) high impregnation and low spreading.

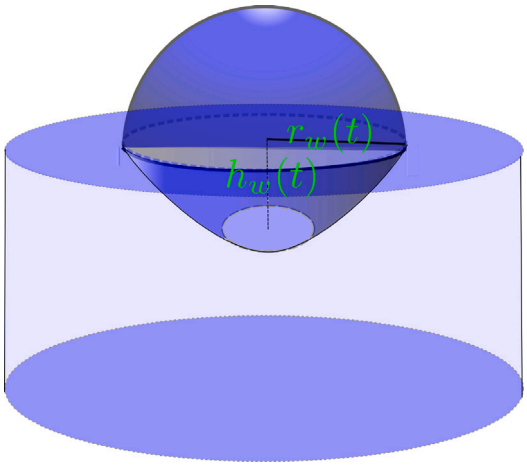

Fig. 2. Model of the competition between the spreading and impregnation of a droplet on/in the powder bed.

2. Theory

2.1. Physical model

The main hypothesis of the proposed model are that the impact velocity of the droplet is null, the ink evaporation is neglected and the effect of temperature is not considered in first approach [27]. The first one is a strong approximation since the droplet speed is given from 5 to 15 m/s by the device manufacturer. Regarding evaporation, the binder is manufactured to be processed at 80 °C. Evaporation (and, more generally, temperature) has a major influence on the evolution of the surface tension and viscosity of the polymer solution used as binder [15,16]. However, the model we have built is fed by parameters identified at 20 °C, leading to these assumptions as a first step to develop our model. Let us consider an ink droplet placed on a bed of powder, whose visible part on the bed is assumed to be a spherical cap of volume $V(t)$ at time t, as described in Fig. 2. The initial volume of the droplet will be considered as the sum of two calculated volumes : the volume of the spherical cap at the surface of the powder bed and the volume impregnated in the porous medium. This droplet evolves under the competition between two phenomena, both due to capillary forces: the droplet spreads on the powder bed, and at the same time, impregnates it. In Fig. 2, $r_w(t)$ denotes the radius of the wet surface at time t, and $h_w(t)$ denotes the position of the flow front into the powder, characterising the spontaneous impregnation of the medium by the binder due to the capillary force.

Let us express the change of the impregnated volume V_p between two instants, t and $t + \Delta t$:

$$V_p(t+\Delta t) - V_p(t) = \int_{\xi=t}^{t+\Delta t} \int_{r=0}^{r_w(t)} 2\pi r \epsilon v_p(r,\xi)\, dr\, d\xi \tag{1}$$

where ϵ is the porosity of the powder bed, v_p is the impregnation rate, assumed to be a function of time and r, the distance to the centre of the wet surface. Note that the radial symmetry of the configuration implies that v_p does not depend on the second polar coordinate, θ. Considering that the wet surface reaches the point of coordinate r at time $\tau(r)$ (*i.e.* $\tau(r)$ is defined by $r_w(\tau(r)) = r$), the impregnation rate is expressed as

$$v_p(r,t) = h_w'(t - \tau(r)) \tag{2}$$

where $h'_w(t) = dh_w(t)/dt$. This choice, already considered by Clarke and coauthors [28] allows us to take into account the delay in the impregnation at point r due to the spreading of the droplet (see Fig. 2).

Combining expression (2) with relation (1) allows us to write, after some manipulations:

$$\frac{dV_p}{dt} = 2\pi\varepsilon \int_0^{r_w(t)} r h'_w(t - \tau(r))\, dr \tag{3}$$

The radius $r_w(t)$ of the wet area can be obtained using literature models [29] or it can be also measured experimentally. Hence, Denesuk and co-authors [13] express the volume $V(t)$ of the spherical cap as a function of the apparent dynamic contact angle, which in turn can be identified by different approaches such as the molecular-kinetic theory [28]. In this work, the radius $r_w(t)$ was determined from goniometric experiments described in Section 3.2.

The impregnated height $h_w(t)$ (or depth in our case) is expressed using the Washburn equation [18], commonly known to describe the spontaneous impregnation of a liquid into a porous medium. This choice is justified by the methodology developed in previous works [30] to experimentally identify parameters describing the wicking of a liquid in fibrous media defined as porous materials. This methodology is here applied to the case of metal powders. Hence, the Washburn equation for porous media is defined as follow:

$$h_w^2(t) = \frac{(c\bar{r})}{2} \frac{\gamma_L \cos\theta_a}{\eta} t \tag{4}$$

with $h_w(t)$, the height (or depth here) of the flow front in the porous medium at time t (see Fig. 2), c, a factor accounting for the tortuosity of the powder, $\bar{r}$, the mean capillary radius, γ_L, the surface tension of the liquid, θ_a, an apparent advancing contact angle, and η, the fluid viscosity. The product $c\bar{r}$, as well as $\cos\theta_a$ were determined by specific experiments of wicking on presintered powder samples (see Section 3.2). As a first approach, it was chosen to keep the traditional modified Washburn homogenised approach [18] with experimental identification rather than the one based on fractal dimensions as developed by Cai et al. [31].

Considering Washburn relation (4), the time derivative of h_w can be expressed. Then, time integration of Eq. (3) provides the impregnated volume as a function of time:

$$V_p(t) = V_{p0} + \pi\varepsilon \sqrt{\frac{c\bar{r}\gamma_L \cos\theta_a}{2\eta}} \int_{\xi=0}^{\xi=t} \int_{r=0}^{r=r_w(\xi)} \frac{r}{\sqrt{\xi - \tau(r)}}\, dr\, d\xi \tag{5}$$

where V_{p0} is the volume of liquid already impregnated at time $t = 0$.

In the analytical model presented in this section, and under the related assumptions, the volume of impregnated liquid expressed by Eq. (5) appears to be mainly determined by a quantity denoted k and defined in Eq. (6). This quantity depends only on the powder and binder properties via the porosity ε and the product $c\bar{r}$, the binder viscosity η and the binder-powder interaction through $\gamma_l \cos\theta_a$. k is assumed to be constant over time.

$$k = \pi\varepsilon \sqrt{\frac{c\bar{r}\gamma_L \cos\theta_a}{2\eta}} \tag{6}$$

Incidentally, note that the proposed approach can be connected to authors previous work [30] defining an equivalence between Darcy and Washburn equations, and is therefore equivalent to the usual models found in the literature based on the Darcy law with capillary pressure [13,28]. Except that the parameters to be identified are different. Hence, assuming now that $h'_w(t)$ is the Darcy velocity and neglecting the gravity force, leads to

$$h'_w(t) = \frac{\kappa}{\varepsilon\eta} \frac{P_{cap}}{h(t)}, \text{ or } h_w^2(t) = \frac{2\kappa}{\varepsilon\eta} P_{cap}\, t \tag{7}$$

where κ is the powder permeability and P_{cap} the capillary pressure. The Darcy–Washburn equivalence exposed in Ref. [30] results in the following description of the capillary pressure:

$$P_{cap} = (c\bar{r})\varepsilon \frac{\gamma_L \cos\theta_a}{4\kappa} \tag{8}$$

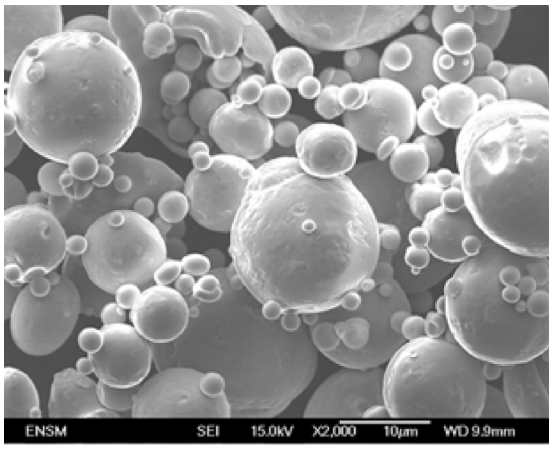

Fig. 3. SEM image of 316L powder used for MBJ presintered samples.

Taking into account (8) in (7) leads to expression (2) and consequently to the same impregnated volume V_p (5).

2.2. Numerical resolution

Let $t_0 = 0, t_1, \ldots, t_N$ be the $N+1$ instants at which the radius of the wet area is obtained from experiments. These data are denoted by r_i: $r_i = r_w(t_i)$, $i = 0, \ldots, N$. Considering these input data, the objective is to compute $V_p(t_n)$ by solving (5). We can write:

$$V_p(t_n) = V_p(t_{n-1}) + \Delta_n V_p \tag{9}$$

and decompose the volume increment $\Delta_n V_p$ as:

$$\Delta_n V_p = k \int_{\xi=t_{n-1}}^{\xi=t_n} \left(\int_{r=0}^{r=r_w(t_{n-1})} \frac{r}{\sqrt{\xi - \tau(r)}}\, dr + \int_{r=r_w(t_{n-1})}^{r=r_w(\xi)} \frac{r}{\sqrt{\xi - \tau(r)}}\, dr \right) d\xi \tag{10}$$

In the right hand side of this expression, the two first time and space integrals can be swapped. The time integral is then evaluated analytically, and the space integral using the trapezoidal rule. In the second double integral, time and space integration cannot be interchanged. Consequently, the time integral is first approximated by the trapezoidal rule, the delay time $\tau(r)$ is approximated by $\tau_m = (t_{n-1} + t_n)/2$, and the space integral is subsequently evaluated analytically:

$$\int_{\xi=t_{n-1}}^{\xi=t_n} \int_{r=r_w(t_{n-1})}^{r=r_w(\xi)} \frac{r}{\sqrt{\xi - \tau(r)}}\, dr\, d\xi \approx \frac{t_n - t_{n-1}}{4} \frac{r_n^2 - r_{n-1}^2}{\sqrt{t_n - \tau_m}}$$

3. Materials and methods

3.1. Materials

Powder and binder used in this study are commercialised by Digital Metal. The powder constituting the powder bed is made of 316L stainless steel. The grains have been characterised as being spherical with sizes between 5 and 25 μm as shown in Fig. 3. The particle size distribution has been estimated by laser granulometry after suspension of the powder in water. Results are summarised in Table 1. The particle sizes referred as $Dv(10)$, $Dv(50)$ and $Dv(90)$ describe that, respectively, 10%, 50% and 90% are smaller than the given value. The *mode* is the most statistically represented particle size and the *span* refers to the distribution of the particle size defined as $(Dv(90) - Dv(10))/Dv(50)$.

The binder, provided by Digital Metal under the denomination C20, was characterised. Its surface tension was measured at 24.5 ± 0.1 mN m^{-1} using the Wilhelmy plate method with a DCAT11 tensiometer

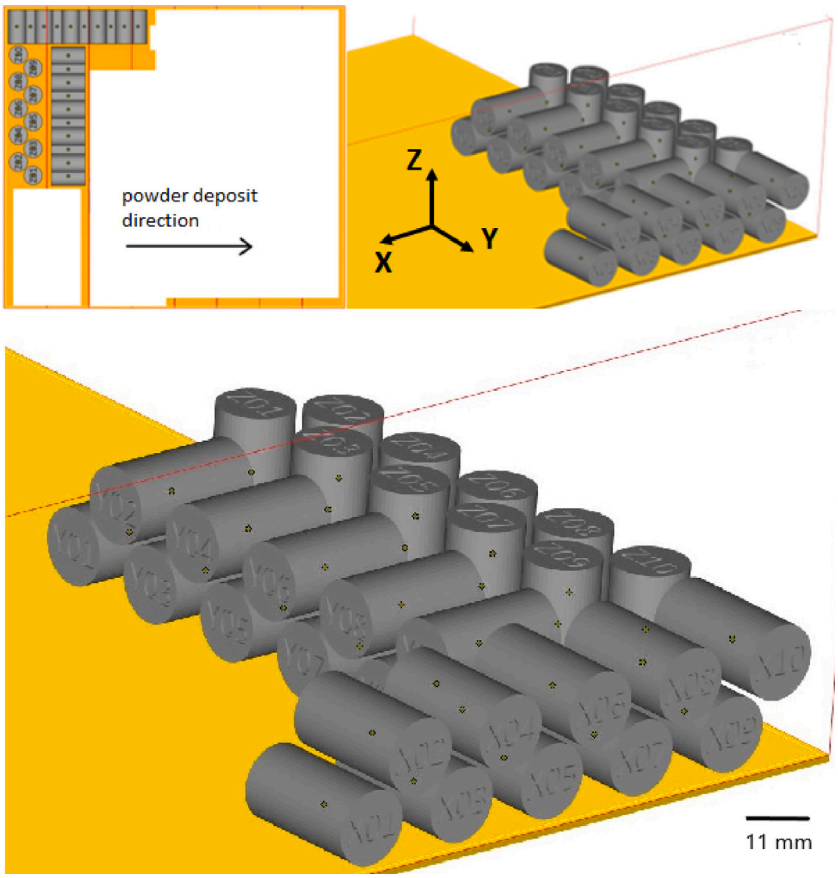

Fig. 4. Illustration of orientation of printed samples in the MBJ set-up.

Table 1
Results from laser granulometry in water.

Dv(10) (μm)	Dv(50) (μm)	Dv(90) (μm)	Mode (μm)	Span (μm)
6.2 ± 0.2	13.9 ± 0.2	26.4 ± 0.4	14.9 ± 0.2	1.4 ± 0.0

Table 2
Properties of liquids used in the study at standard conditions.

	Ink	n-hexane
Viscosity η [Pa s]	2.8×10^{-3}	0.3×10^{-3}
Surface tension γ_L [N/m]	2.45×10^{-2}	1.84×10^{-2}

from Dataphysics [30]. The viscosity of the ink at its initial stage, *i.e.* before any curing, was estimated at 2.8 ± 0.1 mPa s with a Thermo Scientific Haake Rheowin. Pure n-hexane was also used in this study for experimental tests of wicking in pre-fritted powders, allowing to determine the geometric product $c\bar{r}$. Properties of liquids, measured for ink and theoretical for n-hexane, are summarised in Table 2.

Cylindrical samples with a diameter of 11 mm and a height of 20 mm were printed by Metal Binder Jetting (MBJ) using a DMP2000, from Digital Metal. Samples were printed along the main directions of the powder bed in order to verify the isotropy of the additive manufacturing method. Fig. 4 presents a view of the cylinders, captured from the MBJ software. The powder deposition direction corresponds to the X direction in Fig. 4.

Manufactured cylinders were labelled according to the direction of their revolution axis. Two print orientations were considered in this study: cylinders aligned along the X direction or powder deposition direction and cylinders aligned along the transverse Z direction, i.e.the transverse direction to the powder bed deposition. Samples with axis in these directions were labelled X and Z respectively. In order to make these test cylinders easier to handle, to ensure their dimensional stability and to prevent any chemical interaction between cured binder and liquid binder during wetting tests, they were presintered at 900 °C for 30 min under dihydrogen. This thermal treatment leads to remove cured binder and to consolidate the sample without modifying its morphology. The morphology of the presintered samples was verified by measurements in the three main directions and found to be unchanged to a precision down to 1/10 mm. There is a difference between the initial powder bed and the presintered cylinder which lies in the ability of the powder to rearrange itself, as demonstrated by Parab et al. [32]. These effects were neglected in the present study for two reasons: first, the powder content (void ratio) does not change between the powder bed and the presintered samples; second, the impact velocity of the droplet on the powder bed is zero in the model. Indeed, according to the mass and volume measurements, the density was not affected by the pre-sintering step, all samples have a porosity ε of 41%. This porosity was determined by weighing the cylinders and verifying their shape, which allows calculation of their volume. Thus the void content is calculated using the volumetric mass of 316L.

SEM images of the upper surface of those cylinders are shown in Fig. 5. As can be seen on the first image, the cylinder along X, that layers of powder are visible. In comparison to the second image, the cylinder along Z, the surface appears as smoother. This apparent difference in the surface roughness might be the origin of deviation with the model that will be discussed in the results section.

3.2. Methods

3.2.1. Tensiometric tests of wicking

Wicking tests were carried out at standard conditions using a DCAT11 tensiometer from Dataphysics. The tensiometer is equipped

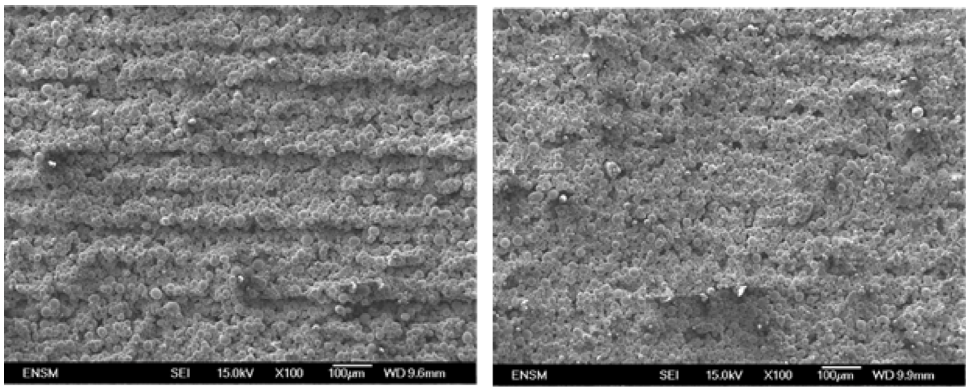

Fig. 5. SEM observation of the upper part of cylinders oriented along X (left) and Z (right).

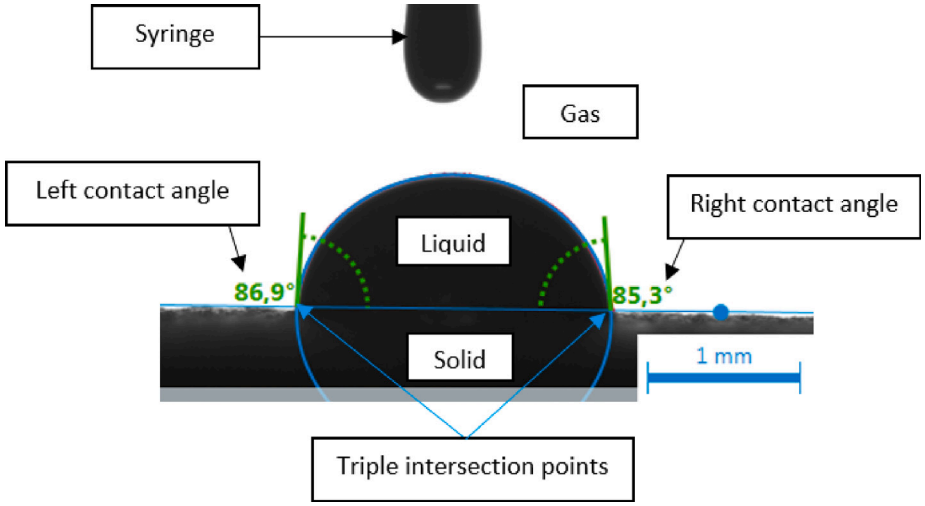

Fig. 6. Description of droplet analysis set up on a drop of ink on presintered sample (Z direction).

with a microbalance having a resolution of 10^{-5} g and an elevator device for the liquid vessel. Presintered samples with suitable size were inserted into a cylindrical sample holder of radius $R = 6$ mm and then clamped to the microbalance. A vessel with the liquid to test is then positioned into the tensiometer and moved up until detection of the sample holder. This instant represents the beginning of the wicking test. The liquid mass gain into the medium as a function of time is recorded. Further details of the experimental protocol are given in previous works [30]. According to the Washburn theory (Eq. (4)), the squared mass gain varies linearly as a function of time, as following:

$$m^2(t) = \frac{(c\bar{r})\epsilon^2(\pi R^2)^2}{2}\frac{\rho^2\gamma_L\cos\theta_a}{\eta}t \tag{11}$$

where ρ is the liquid density. The product $(c\bar{r})$, characterising the geometry of the medium, was obtained by performing wicking tests with n-hexane assumed to be totally wetting (the apparent contact angle in Eq. (11) is approximated to zero). If Washburn assumptions are verified [30,33], $c\bar{r}$ is then determined from the linear fit of the recorded curve $m^2(t)$ versus t and Eq. (11). Once this quantity was known, wicking tests were conducted with the binder, in order to estimate the apparent contact angles ($\cos\theta_a$), again from a linear fit of the recorded $m^2(t)$ curves with Eq. (11). Four tests for each direction of sample (X and Z) and for each liquid (n-hexane and ink) were carried out. These experiments made it possible to determine the parameters involved in Eq. (6) for the identification of the factor k.

3.2.2. Goniometric tests of droplet spreading and imbibition

A goniometer KRŰSS DSA30 (Drop shape analyzer) was used to monitor the spreading and impregnation of ink droplets on presintered samples. In this approach, a drop of 3 µL of the test liquid (ink) is deposited on the upper surface of the cylindrical sample with a syringe controlled by the drop shape analyzer. A picture of the test is shown in Fig. 6. By using a high-speed camera, the average contact angle and the volume of the drop are recorded as functions of time [34,35]. The average contact angle is the average between the two angles, right and left, at the triple intersection points (intersection points between the three phases: liquid, solid and gas). The software ADVANCE v.1.9.2.3 was used for data acquisition and processing. Images were acquired with a high-speed and high-resolution camera (reference CF03) from IDS Imaging Development Systems. Following steps of the test, the camera performs an acquisition of the evolution of the droplet with a frequency of 120 fps (frame per second).

As for wicking, two directions were studied to evaluate spreading as a function of printing direction: X, the direction of powder bed deposition and Z, that is the transverse direction to the powder bed. Four drop tests were performed for each direction to assess the test repeatability. These tests allowed to determine the radius of the wet surface $r_w(t)$, the drop volume $V(t)$ and the average contact angle of spreading as a function of time.

4. Results

4.1. Wicking on presintered samples

According to the method detailed in Section 3.2.1, wicking tests were carried out first with n-hexane and then with the binder in presintered cylinders, assuming unidirectional flow along their revolution

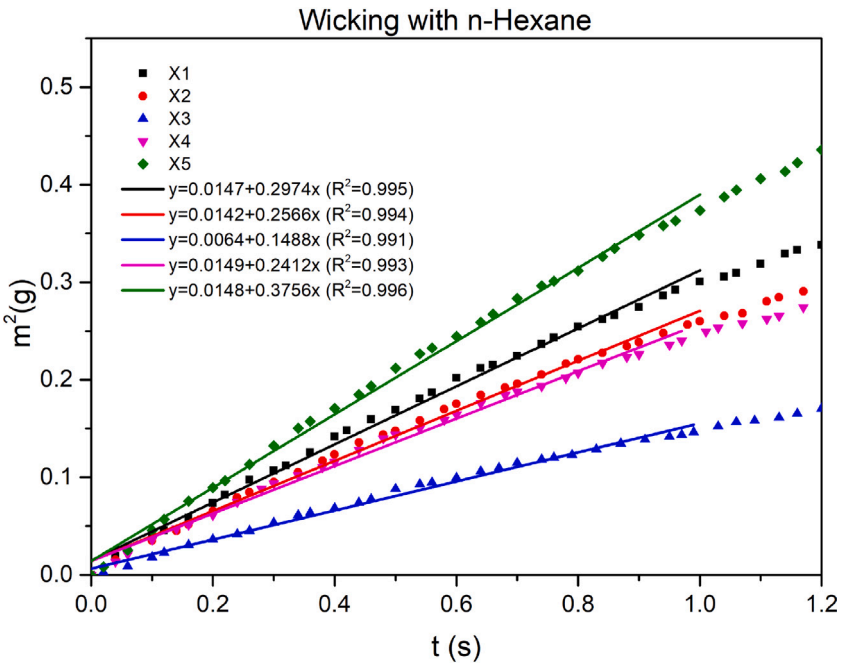

Fig. 7. Wicking curves (mass vs. time) and linear fits for presintered samples with n-Hexane along X.

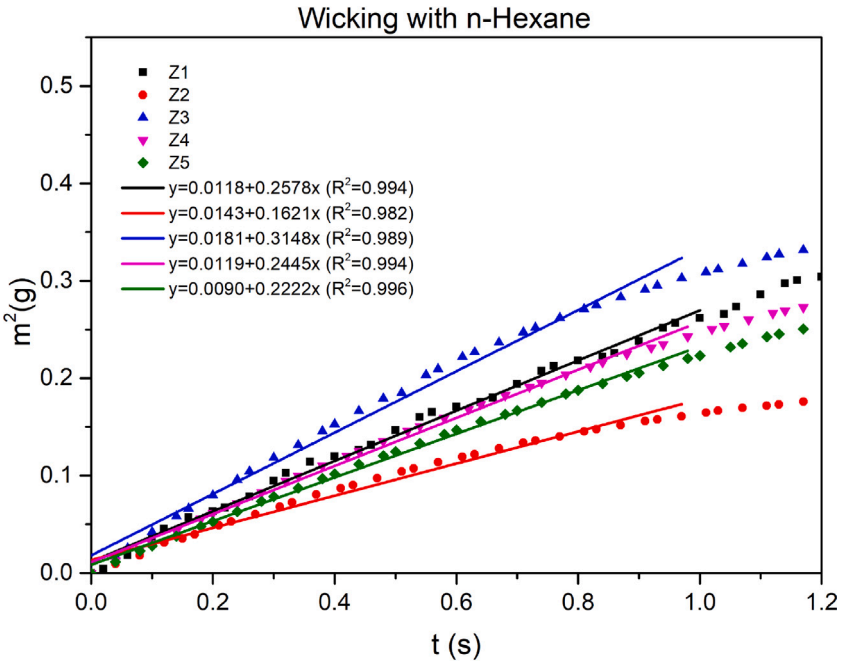

Fig. 8. Wicking curves (mass vs. time) and linear fits for presintered samples with n-Hexane along Z.

axis oriented along to the X and Z directions of the manufacturing process, as shown in Fig. 4.

Wicking curves of squared mass gain as a function of time are shown in Figs. 7 and 8 for n-hexane in the X and Z directions respectively.

It can be seen that the trends are linear (with correlation coefficients close to 1) and thus in accordance with the Washburn theory. The linear regressions have not been forced to cross the origin of the graph to verify the accordance with the Washburn equation. This data (deviation from origin) is used to estimate the dispersion on values calculated for the slope. The assumption of a zero contact angle with n-hexane allows the calculation of the parameter $c\bar{r}$. Values of this parameter, obtained from the linear fit slopes are summarised in Table 3. It can be seen that, considering the dispersion, there is no significant difference between the two directions of printing. A slightly higher value can be seen along Z being the transverse direction of the powder bed.

Table 3
$c\bar{r}$ averaged on five presintered samples for X and Z directions.

	X	Z
$c\bar{r}$ [10^{-5} m]	1.27 ± 0.38	1.55 ± 0.36

Wicking tests carried out with the printing ink are shown in Figs. 9 and 10 for the two directions. Linear fit of the squared mass still gives very high correlation coefficients. Although it can be noticed

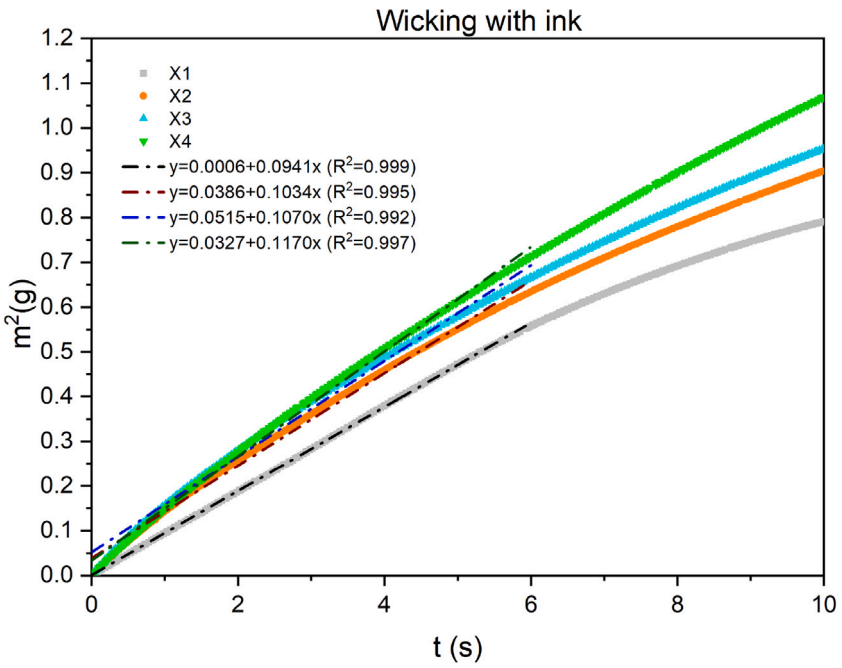

Fig. 9. Wicking curves (mass vs. time) and linear fits for presintered samples with the binder along X.

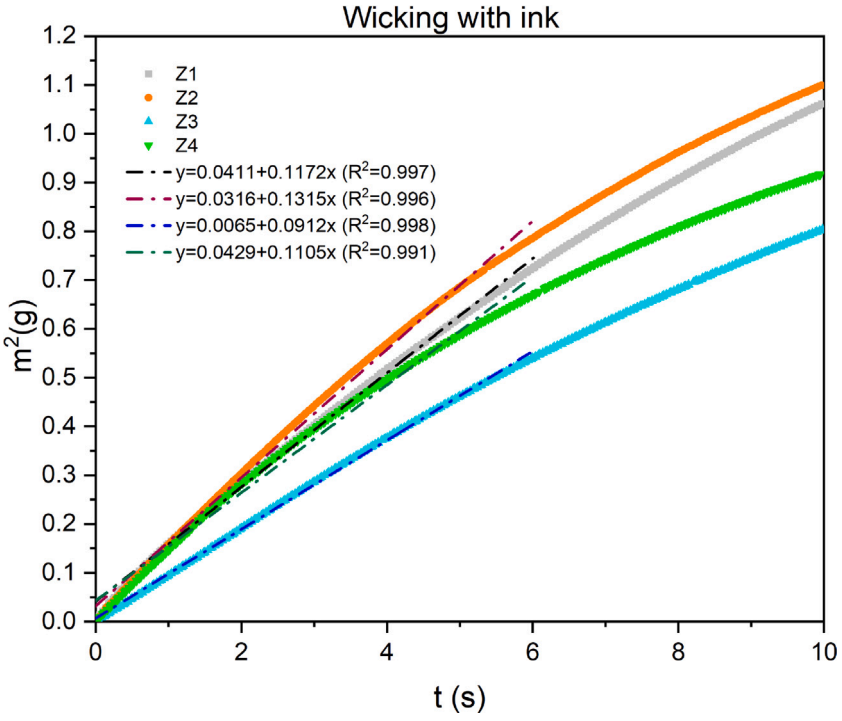

Fig. 10. Wicking curves (mass vs. time) and linear fits for presintered samples with the binder along Z.

that, at the beginning of wicking, the linear fit deviates slightly from the experimental values. With the previously obtained values of the geometric products ($c\bar{r}$) and the slope of the linear fit, the values of the $\cos\theta_a$ from Washburn equation were calculated. Those values are summarised in Table 4. It can also be noticed that the linear fit is valid for appreciatively 1 s for n-hexane and 6 s for binder. If linear fit with n-hexane cannot be linked to process duration, the sorption time of a printed droplet (shorter than 6 s) leads to consider that the values are relevant for the duration of the process. The first obvious comment on Table 4 is that the cosine value is higher than 1. This is due to the fact that this parameter in Washburn was originally the cosine of an angle in a tube but for the modified equation for porous media, it is a parameter that is not related to an actual angle. Then, it can be observed that the results in the X and Z directions are significantly different. The $\cos\theta_a$ for the Z direction is very high, more than the double compared to the X direction. This could imply that during the process the impregnation rate of ink is higher in the Z direction than in the direction of the powder bed deposition. This could lead to the assumption that the "b" configuration of Fig. 1 prevails. This assumption will be verified in the next sections, thanks to the newly developed model.

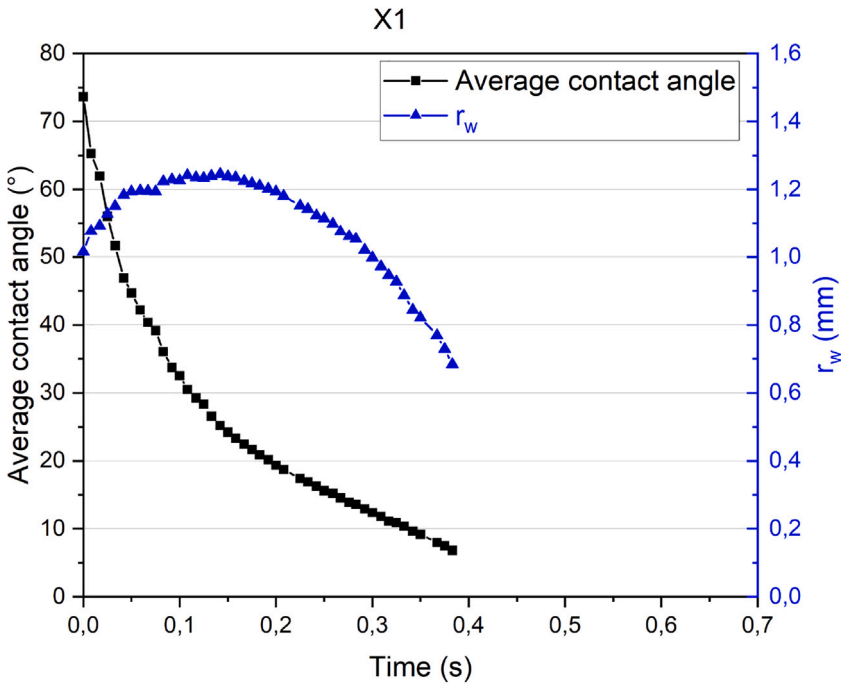

Fig. 11. Raw data of average contact angle against time (X-direction).

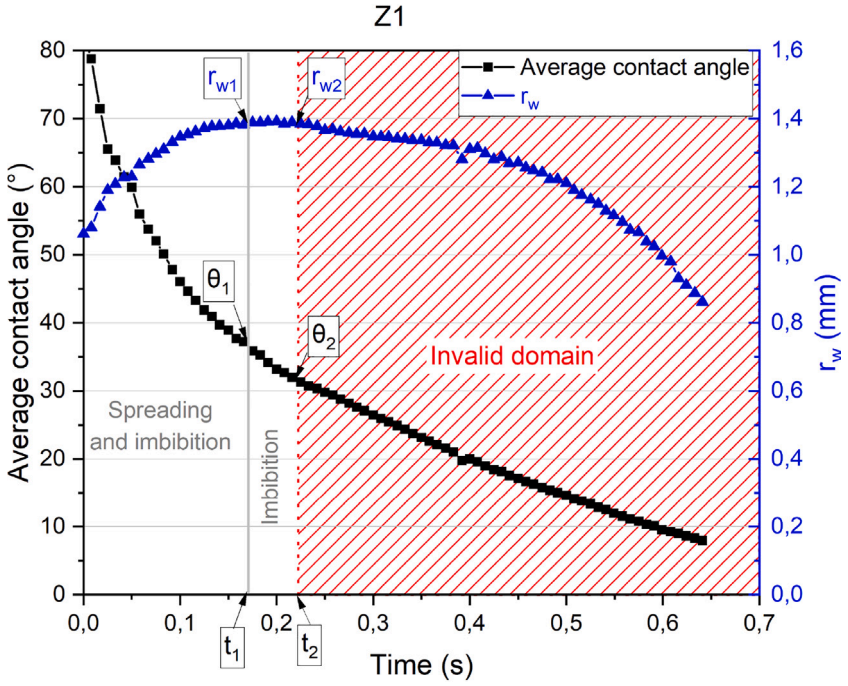

Fig. 12. Average contact angle against time with definition of characteristic times for modelling (Z-direction).

Table 4
$\cos\theta_a$ averaged on four presintered samples for the X and Z directions.

	X	Z
$\cos\theta_a$	1.51 ± 0.02	3.74 ± 0.56

4.2. Droplet spreading and imbibition on presintered samples

According to the method detailed in Section 3.2.2, droplets of ink were deposited on the upper surface of the presintered samples. The general appearance of the curves of the average contact angle and the radius r_w as a function of time are shown in Figs. 11 (X-direction) and 12 (Z-direction).

Raw results are shown in Fig. 11. Three areas can be described on these curves and they are displayed on Fig. 12. In the first area, the radius r_w increases until time t_1, mainly due to the spreading phenomenon, while the contact angle gradually decreases. Both phenomena of spreading and impregnation are thus occurring. Beyond t_1 the radius r_w remains constant, between times t_1 and t_2, and indicates that the spreading phase is over. However, the average contact angle continues to decrease due to the imbibition phenomenon only. For t

Table 5
Time, θ and r_w on four presintered samples for the directions X and Z.

	θ_{in} [°]	r_{win} [mm]	t_1 [s]	θ_1 [°]	r_{w1} [mm]
X1	73.7	1.01	0.10	32.5	1.23
X2	74.8	1.01	0.13	31.2	1.16
X3	76.7	1.08	0.13	32.2	1.29
	75.1 ± 1.5	1.03 ± 0.04	0.12 ± 0.02	32.0 ± 0.7	1.23 ± 0.06
Z1	82.7	1.06	0.15	38.9	1.38
Z2	88.5	0.99	0.16	43.5	1.17
Z3	85.4	1.01	0.21	36.1	1.33
	85.5 ± 2.9	1.02 ± 0.04	0.17 ± 0.03	39.5 ± 3.7	1.29 ± 0.11
			t_2 [s]	θ_2 [°]	r_{w2} [mm]
X1			0.17	22.5	1.22
X2			0.16	27.6	1.16
X3			0.21	22.6	1.28
			0.18 ± 0.03	24.2 ± 2.9	1.22 ± 0.06
Z1			0.23	30.7	1.38
Z2			0.23	35.9	1.17
Z3			0.28	30.3	1.33
			0.25 ± 0.03	32.3 ± 3.1	1.30 ± 0.11

$> t_2$, the radius curve shows an unexpected behaviour : it decreases instead of keeping constant. This can be explained by observing the droplet in Fig. 13, which corresponds to a time slightly higher than t_2. Light reflection is observed at both right and left triple intersection points, and thus leading to an invalid estimation of the contact angle. The associated error of measurement increases as the average contact angle decreases, affecting directly the reading of the radius and contact angle values. Consequently, the dot line at t_2 correspond to the last time of the domain of validity with the goniometric method. θ_2 is thus the minimum contact angle detectable.

Results obtained from goniometric tests are shown in Table 5. By taking into account only times before t_2, the following parameters were determined : the initial contact angle (θ_{in}) and the initial radius (r_{win}), corresponding to the initial time t_0; the contact angle θ_1 and the radius (r_{w1}), corresponding to the last points of the spreading and imbibition area (at t_1) and the contact angle θ_2 and the radius (r_{w2}), corresponding to the last valid points (at t_2). Through the observation of the radius evolution, the spreading phenomenon begins at t_0 and finishes at t_1. But, for the imbibition phenomenon, it is not possible to determine the initial and the final point : between t_0 and t_1, it is a coupled phenomenon and, after t_2, the imbibition continues cannot be characterised by goniometric method. As the initial volume deposited on the cylinder in the X and Z directions is the same (3 µL), differences of contact angle between both directions observed at t_0, t_1 and t_2 are probably due to the difference of surface roughness of the cylinders in the X and Z directions (Fig. 5). This surface difference could modify the shape and the kinetic of spreading of the droplet and, consequently, the contact angle. These average contact angles obtained experimentally were used to determined the V(t) (Eq. (12)) for the confrontation of the numerical model with experimental results.

4.3. Comparison of the model with experiments

The binder behaves as a Newtonian fluid during the spreading and imbibition of the droplet. Its viscosity and surface tension were determined at room temperature. These values, given in Table 2, do not depend on X and Z directions along which the presintered samples have been designed. Similarly, the porosity ε was found to be equal to 0.41 regardless the direction considered. In contrast, the impregnation kinetic and the associated parameters $c\bar{r}$ and $\cos\theta_a$ depend on this direction (see Tables 3 and 4). Note that, as already mentioned, the parameter called $\cos\theta_a$ is greater than 1. This parameter can only be unambiguously interpreted as the cosine of a contact angle in the case of capillary rise against a wall or in a tube with a well-localised meniscus. The situation is geometrically more complex in the case of impregnation of a porous medium, such as powder, by a liquid: $\cos\theta_a$ is then only considered as a parameter describing the ink-powder interaction, not considering an actual angle.

Table 6
Theoretical values of k obtained by Eq. (6) with parameters provided in Tables 2 and 3 and 4 and $\varepsilon = 0.41$ for directions X and Z: mean, minimum and maximum values.

k_{th}	X	Z
MEAN	1.2×10^{-2}	2.1×10^{-2}
MIN	9.8×10^{-3}	1.7×10^{-2}
MAX	1.4×10^{-2}	2.5×10^{-2}

The questions to be answered are: Does the volume of impregnated ink evolves as described by the theoretical model (5)? If so, is the constant k well predicted by Eq. (6)? The values of this "theoretical" k, denoted k_{th} and reported in Table 6, are calculated with the parameters mentioned above, taking into account their standard deviations to obtain minimal and maximal values. In addition, from the experimental measurements over time of the volume $V(t)$ of the visible part of the droplet on the powder bed, $V_p(t)$ the volume of the impregnated ink, as well as $r_w(t)$ the radius of the wet area, can be deduced thanks to the assumptions made in Section 2. On the one hand, neglecting evaporation allows the calculation of $V_p(t)$, while on the other hand, assuming that the droplet is a spherical cap leads to the following relation between $V(t)$ and $r_w(t)$:

$$V(t) = \frac{\pi r_w(t)^3 (2 + \cos\theta(t))(1 - \cos\theta(t))}{3 \sin\theta(t)(1 + \cos\theta(t))} \tag{12}$$

where the apparent angle $\theta(t)$ made by the droplet on the powder bed has been measured by the goniometric method in Section 4.2. By using least squares to minimise the difference between the experimental volume $V_p(t)$ and the volume from Eq. (5), we can then obtain an "experimental" value of k, denoted k_{exp}, for each of the twelve presintered samples, grouped in three series according to whether they were aligned along X or Z. Consequently, as in Section 4.2, values of k_{exp} for X and Z directions are presented in Table 7. Figs. 14 and 15 show, respectively for the X and Z directions, the volume of binder impregnated as a function of time, from experimental measurements and from Eq. (5) with $k = k_{exp}$.

The first remark that can be made concerns the very different behaviour observed in Figs. 14 and 15. Four samples are displayed in each graph and those samples correspond to the presintered cylinders shown in Figs. 9 and 10 for the main direction X and Z respectively. A very small dispersion of the experimental results (and thus of the model) is observed in Fig. 14: when the curves are brought back to the same origin, they are almost superimposed, with small fluctuations. In

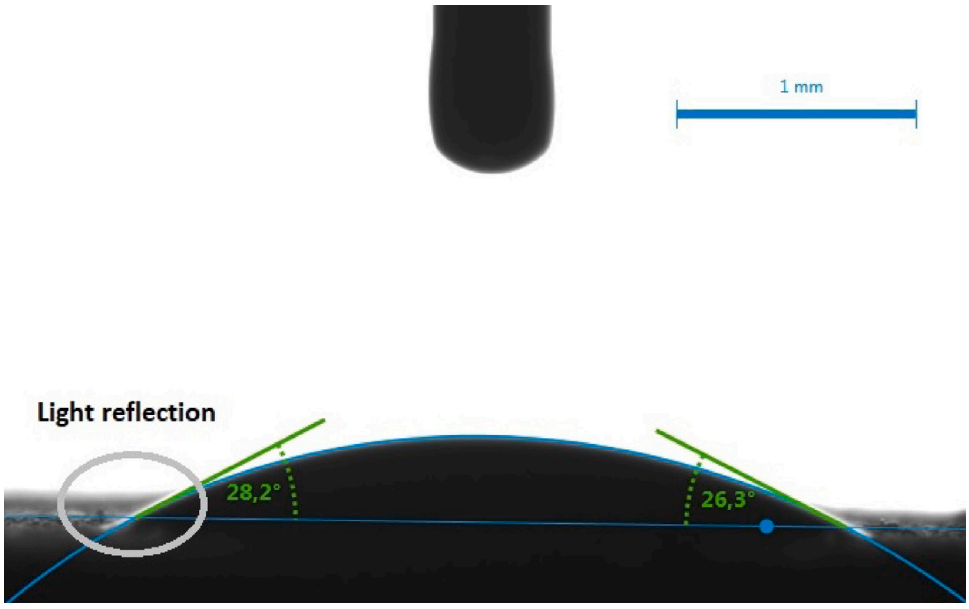

Fig. 13. Illustration of the angle definition issue due to light reflection (sample X1).

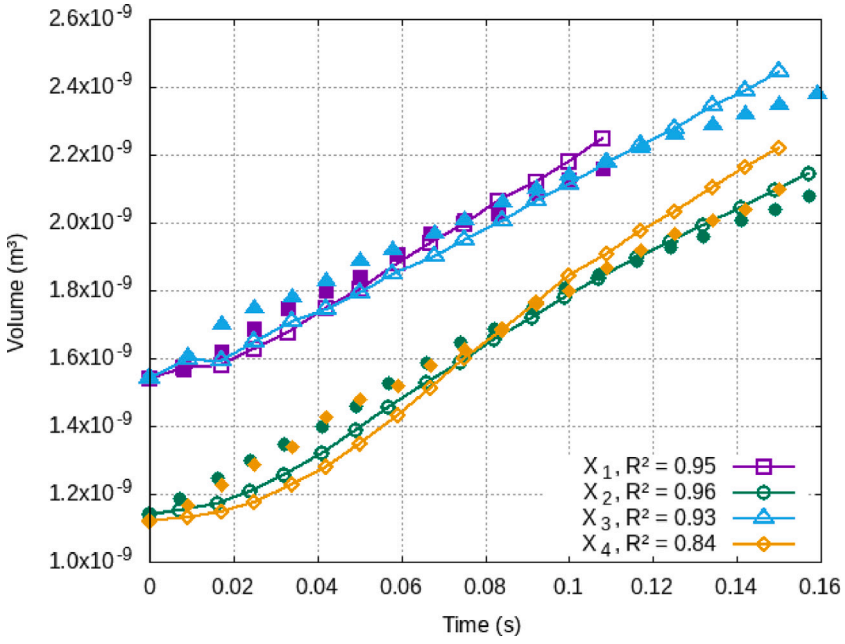

Fig. 14. The four samples constructed along X. Evolution of the volume of impregnated ink. Filled point symbols: experimental volumes. Lines with empty point symbols: volumes given by Eq. (5) with $k = k_{exp}$ of Table 7.

Table 7
Values of $k = k_{exp}$ obtained by least squares fitting the volume provided by Eq. (5) with the experimentally measured volume, for three series (constructed along X and Z respectively) of four samples each. The R^2 estimator is also given.

k_{exp}	X	R^2	Z	R^2
#1	7.3×10^{-3}	0.95	3.5×10^{-3}	0.98
#2	4.8×10^{-3}	0.96	1.0×10^{-2}	0.87
#3	1.1×10^{-2}	0.93	7.8×10^{-3}	0.997
#4	8.4×10^{-3}	0.93	3.23×10^{-3}	0.95
MEAN	7.9×10^{-3}		6.1×10^{-3}	

this case, the average value of k_{exp} obtained, $\bar{k}_{exp} = 7.9 \times 10^{-3}$ seems relevant to describe the four curves. This value is of the same order as the theoretical value obtained k_{th}. It can be concluded that the model (Eq. (5)) correctly reproduces the impregnation of the drop for the X direction. The differences with experiment can be explained by the assumptions of the model (the droplet is assumed to be a spherical cup) and the fact that surface roughness is not taken into account.

In contrast, Fig. 15 shows a strong dispersion of the results: each of the curves presents a different impregnation rate. Even in this situation, each curve seems to behave as predicted by the model (5), but with its own value of k_{exp} (with an exception for test Z_2, with a larger deviation). Of course the mean value $\bar{k}_{exp}$ is no longer relevant to characterise the time evolution of the volume of impregnated ink. Furthermore, this mean value is 4 times smaller than the smallest theoretical value. Hence, the faster impregnation predicted in Section 4.1 for the Z direction (k_{th} for Z is 2 times that for X) is not confirmed here. However, according to Fig. 4, the surface roughness of cylinders built

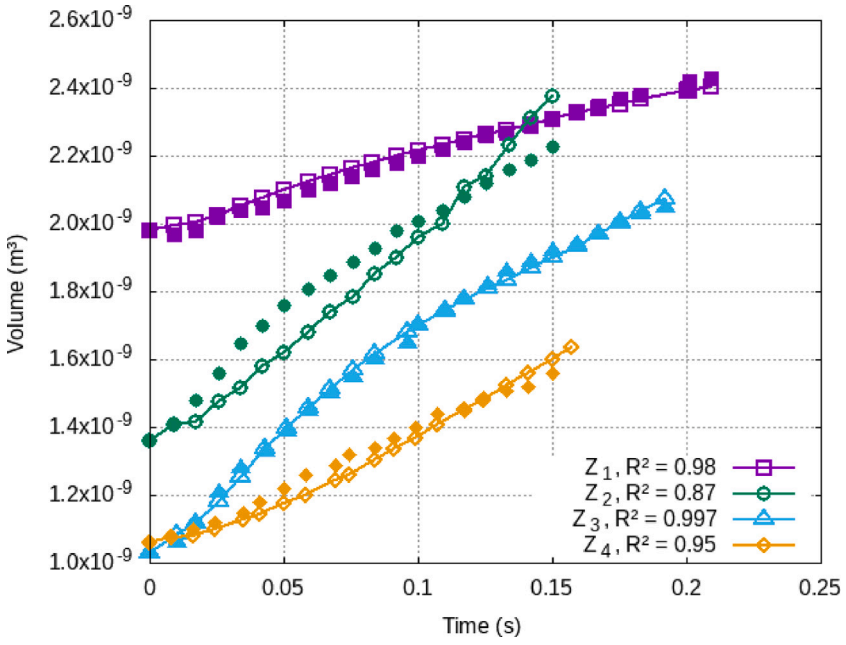

Fig. 15. The four samples constructed along Z. Evolution of the volume of impregnated ink. Filled point symbols: experimental volumes. Lines with empty point symbols: volumes given by Eq. (5) with $k = k_{exp}$ of Table 7.

in Z direction is drastically different from that of the cylinders in the X and Y directions, since the surface has striations perpendicular to the Z axis, *i.e.* to the spreading direction. It can be assumed that this changes the behaviour of the droplet, in particular its impregnation rate, and explains the dispersion shown in Fig. 15. Moreover, regarding Eq. (5), the impregnation rate given by the theoretical model writes

$$\frac{dV_p}{dt}(t) = k \int_{r=0}^{r=r_w(t)} \frac{r}{\sqrt{t-\tau(r)}}\, dr \tag{13}$$

It can then be argued that taking into account the presence of striation will modify the integral term in a way to be defined by further studies. Without this modification, the proposed model is incomplete for the Z direction. However, the determination of k_{exp} from the experimental curves by the method of least squares, "forces" the value of k_{exp} to include this change, resulting in values smaller than the theoretical values.

5. Conclusion

This study on binder impregnation, corresponding to the basis of the 3D printing process of Metal Binder Jetting, has highlighted an orthotropy in the imbibition. Indeed, it was shown that, considering wicking in presintered cylinders, the fastest impregnation rate is along the Z-axis, *i.e.* transversely to the powder deposition in the stack. This indicates that a drop of ink will tend to go deeper in the powder bed, with limited spreading in the in-plane directions. A model considering the competition between droplet spreading and imbibition of the ink in the powder bed was developed. The expected trend of impregnated volume evolution was observed experimentally, and experimental data were successfully fitted by the model. However, a ratio of two between in-plane and transverse imbibition kinetics found in the experimental wicking, was not predicted by the model. This could be due to the fact that surface properties have a significant influence on droplet spreading. Indeed, presintered cylinders have micro-stripes due to powder stacking in the MBJ process. Surface roughness effects are not taken into account in the model described in this study. Further studies will focus on adapting the model to include spreading parameters and developing associated characterisation test. Adaptation of the model to include parameters related to temperature, evaporation of the binder, velocity of the droplet and differences between MBJ devices will also be needed. Manufacturing a powder bed representative to the MBJ process will also be an issue to solve in future works.

These observations can be related to the process by considering that the ink flow is easier between the plies of the powder bed than in-plane. Indeed, to prevent brittleness of the unsintered parts, the parts of minimum width should be oriented along the Z direction in order to maximise their ink content and therefore their stability during sintering. Relation between maximum impregnation and toughness of the part before sintering is yet to be demonstrated since the powder layering will also have an influence on this parameter. Further work will focus on verifying this hypothesis by manufacturing specific parts with tailored areas of small width along different directions, and modelling both ink impregnation and residual stresses to predict failure of the unsintered parts.

CRediT authorship contribution statement

Romain Ravel: Writing – original draft, Methodology, Investigation, Formal analysis. **Monica Francesca Pucci:** Conceptualization, Methodology, Validation, Investigation, Formal analysis, Writing – review & editing. **Synthia Divin:** Investigation, Methodology. **Benoît Verquin:** Project administration, Funding acquisition, Methodology. **Christophe Reynaud:** Project administration, Funding acquisition, Methodology. **Julien Bruchon:** Conceptualization, Project administration, Funding acquisition, Supervision, Formal analysis, Writing – review & editing. **Pierre-Jacques Liotier:** Conceptualization, Project administration, Funding acquisition, Supervision, Formal analysis, Writing – review & editing.

Declaration of competing interest

The authors declare that they have no known competing financial interests or personal relationships that could have appeared to influence the work reported in this paper.

Data availability

Data will be made available on request.

References

[1] B. Utela, D. Storti, R. Anderson, M. Ganter, A review of process development steps for new material systems in three dimensional printing (3DP), J. Manuf. Process. 10 (2) (2008) 96–104.

[2] I. Rishmawi, M. Salarian, M. Vlasea, Tailoring green and sintered density of pure iron parts using binder jetting additive manufacturing, Addit. Manuf. 24 (2018) 508–520.

[3] A. Mostafaei, A.M. Elliott, J.E. Barnes, F. Li, W. Tan, C.L. Cramer, P. Nandwana, M. Chmielus, Binder jet 3D printing—Process parameters, materials, properties, modeling, and challenges, Prog. Mater. Sci. 119 (2021) 100707.

[4] M. Ziaee, N.B. Crane, Binder jetting: A review of process, materials, and methods, Addit. Manuf. 28 (2019) 781–801.

[5] B. Liu, R. Wildman, C. Tuck, I. Ashcroft, R. Hague, Investigation the effect of particle size distribution on processing parameters optimisation in selective laser melting process, in: 2011 International Solid Freeform Fabrication Symposium, University of Texas at Austin, 2011.

[6] A.M. Elliott, P. Nandwana, D. Siddel, B. Compton, A method for measuring powder bed density in binder jet additive manufacturing process and the powder feedstock characteristics influencing the powder bed density, in: 2016 International Solid Freeform Fabrication Symposium, University of Texas at Austin, 2016.

[7] T. Colton, N.B. Crane, Influence of droplet velocity, spacing, and inter-arrival time on line formation and saturation in binder jet additive manufacturing, Addit. Manuf. 37 (2021) 101711.

[8] Y. Mao, J. Li, W. Li, D. Cai, Q. Wei, Binder jetting additive manufacturing of 316L stainless-steel green parts with high strength and low binder content: Binder preparation and process optimization, J. Mater Process. Technol. 291 (2021) 117020.

[9] M. Vaezi, C.K. Chua, Effects of layer thickness and binder saturation level parameters on 3D printing process, Int. J. Adv. Manuf. Technol. 53 (1) (2011) 275–284.

[10] M. Waris, P.-J. Liotier, S. Drapier, Effect of the mold on the residual strain field monitored with optical fibers sensors in resin transfer molding processes, J. Compos. Mater. 48 (21) (2014) 2589–2601.

[11] K.P. Hapgood, J.D. Litster, S.R. Biggs, T. Howes, Drop penetration into porous powder beds, J. Colloid Interface Sci. 253 (2) (2002) 353–366.

[12] H. Miyanaji, S. Zhang, L. Yang, A new physics-based model for equilibrium saturation determination in binder jetting additive manufacturing process, Int. J. Mach. Tools Manuf. 124 (2018) 1–11.

[13] M. Denesuk, G. Smith, B. Zelinski, N. Kreidl, D. Uhlmann, Capillary penetration of liquid droplets into porous materials, J. Colloid Interface Sci. 158 (1) (1993) 114–120.

[14] M. Denesuk, B. Zelinski, N. Kreidl, D. Uhlmann, Dynamics of incomplete wetting on porous materials, J. Colloid Interface Sci. 168 (1) (1994) 142–151.

[15] S.I. Yanez-Sanchez, M.D. Lennox, D. Therriault, B.D. Favis, J.R. Tavares, Model approach for binder selection in binder jetting, Ind. Eng. Chem. Res. 60 (42) (2021) 15162–15173.

[16] D.A. Schlachter, M.D. Lennox, B.D. Favis, D. Therriault, J.R. Tavares, Physico-chemical limitations of capillary models applied to high-concentration polymer solutions, ACS Omega 7 (7) (2022) 5636–5645.

[17] S. Im, R. Batmaz, A. Natarajan, É. Martin, Compatibility study of polymeric binders for aluminum binder jet parts, in: Light Metals 2023, Springer, 2023, pp. 471–477.

[18] E.W. Washburn, Note on a method of determining the distribution of pore sizes in a porous material, Proc. Natl. Acad. Sci. USA (1921) 115–116.

[19] S.M. da Silva, J. Oliveira, Cork powders wettability by the Washburn capillary rise method, Powder Technol. 387 (2021) 16–21.

[20] V. Carretier, M.F. Pucci, C. Lacoste, A. Regazzi, J.-M. Lopez-Cuesta, An efficient solution to determine surface energy of powders and porous media: Application to untreated and treated lignin, Appl. Surf. Sci. 579 (2022) 152159.

[21] S.-Y. Chun, T. Kim, B. Ye, B. Jeong, M.-j. Lee, D.H. Lee, E.-S. Kim, H. Lee, H.-D. Kim, Capillary pressure and saturation of pore-controlled granules for powder bed binder jetting, Appl. Surf. Sci. 515 (2020) 145979.

[22] J. Marston, J.E. Sprittles, Y. Zhu, E. Li, I.U. Vakarelski, S.T. Thoroddsen, Drop spreading and penetration into pre-wetted powders, Powder Technol. 239 (2013) 128–136.

[23] J. Bruchon, Y. Liu, N. Moulin, Finite element setting for fluid flow simulations with natural enforcement of the triple junction equilibrium, Comput. & Fluids 171 (2018) 103–121.

[24] M. Yeager, P. Simacek, S.G. Advani, Prediction of micro impregnation phenomena in additively manufactured composite materials, Composites A 156 (2022) 106861.

[25] D. Legendre, M. Maglio, Numerical simulation of spreading drops, Colloids Surf. A 432 (2013) 29–37.

[26] H. Tan, Three-dimensional simulation of micrometer-sized droplet impact and penetration into the powder bed, Chem. Eng. Sci. 153 (2016) 93–107.

[27] M. Choi, G. Son, W. Shim, Numerical simulation of droplet impact and evaporation on a porous surface, Int. Commun. Heat Mass Transfer 80 (2017) 18–29.

[28] A. Clarke, T. Blake, K. Carruthers, A. Woodward, Spreading and imbibition of liquid droplets on porous surfaces, Langmuir 18 (2002) 2980–2984.

[29] P.-G. De Gennes, Wetting: statics and dynamics, Rev. Modern Phys. 57 (3) (1985) 827.

[30] M.F. Pucci, P.-J. Liotier, S. Drapier, Capillary wicking in a fibrous reinforcement–Orthotropic issues to determine the capillary pressure components, Composites A 77 (2015) 133–141.

[31] J. Cai, B. Yu, A discussion of the effect of tortuosity on the capillary imbibition in porous media, Transp. Porous Media 89 (2) (2011) 251–263.

[32] N.D. Parab, J.E. Barnes, C. Zhao, R.W. Cunningham, K. Fezzaa, A.D. Rollett, T. Sun, Real time observation of binder jetting printing process using high-speed X-ray imaging, Sci. Rep. 9 (1) (2019) 1–10.

[33] M.F. Pucci, P.-J. Liotier, S. Drapier, Capillary wicking in flax fabrics–effects of swelling in water, Colloids Surf. A 498 (2016) 176–184.

[34] Z. Wang, L. Espín, F.S. Bates, S. Kumar, C.W. Macosko, Water droplet spreading and imbibition on superhydrophilic poly (butylene terephthalate) melt-blown fiber mats, Chem. Eng. Sci. 146 (2016) 104–114.

[35] M.F. Pucci, B. Duchemin, M. Gomina, J. Bréard, Temperature effect on dynamic wetting of cellulosic substrates by molten polymers for composite processing, Composites A 114 (2018) 307–315.